Rock Mech Rock Eng
DOI 10.1007/s00603-013-0370-2

ORIGINAL PAPER

# Damage and Permeability Development in Coal During Unloading

**Hai-Dong Chen · Cheng Yuan-Ping · Hong-Xing Zhou · Wei Li**

Received: 16 October 2012 / Accepted: 7 January 2013


**Abstract** One of the key issues in protective seam mining is the pressure relief and permeability improvement effect. In this paper, the results of X-ray CT scanning experiments and permeability experiments using reconstituted coal specimens subjected to the same stress path and the same effective confining pressure (confining pressure minus pore pressure) are combined using the stress–strain relationship to study the damage to reconstituted coal specimens and its influence on permeability during the unloading process. When the effective confining pressure ($\sigma_3 - p$) is unloaded from 8 to 6 MPa and the deviatoric stress increases, the damage variables will increase by 0.0351 and 0.084, respectively, compared with the unloading point under the fixed axial displacement with unloading confining pressure (FADUCP) and fixed deviatoric stress with unloading confining pressure (FDSUCP) stress paths. At the same time, the permeability increased by 1.7 and 16.7 %, respectively. Therefore, the damage variable and permeability increased notably little in this process. After the effective confining pressure is unloaded to approximately 5 MPa, together with the decrease in the deviatoric stress, the growth of the damage variable and permeability begins to accelerate. In addition, the relative decrease in the deviatoric stress with appearing damage cracks, and the relative increase in permeability with the same amount of effective confining pressure being unloaded, shows that the damage to specimens under the FDSUCP stress path is larger than that from the FADUCP stress path.

**Keywords** Protective seam mining · Unloading · Reconstituted coal · X-ray CT scan · Permeability

## 1 Introduction

Over many years, work on the topic of gas prevention in coal mines has shown that for a coal seam group that has a risk of coal and gas outbursts, extraction of protective seams is the most economical and effective measure (Lama and Bodziony 1998; Liu et al. 2011; Wang and Cheng 2012). This intervention not only insures the safe and efficient recovery of seams, but also improves the capture rate of coal bed methane (CBM), which plays an important role in promoting energy conservation and comprehensive utilization of resources.

Extraction of protective seams causes a reduction in the three-dimensional stress in the surrounding rock, and this reduction varies for different distances to the protective seams (Yang et al. 2011a, b; Guo et al. 2012). The change in stress state causes damage to the surrounding rock, which increases the permeability. The cave zones, fracture zones, and continuous deformation zones are classified according to the different permeability (Palchik 1989; Karacan et al. 2007). Specifically, Palchik (2003, 2005) studied the formation process and the scope of the fractured zone in a long-wall mining face. Majdi et al. (2012) put forward a mathematical model for the height of the distressed zone. Also, Yang TH et al. (2011) put forward a stress-damage-flow coupling model and applied it to pressure relief CBM in deep coal seams.

H.-D. Chen · C. Yuan-Ping (✉) · H.-X. Zhou · W. Li
National Engineering Research Center for Coal and Gas Control,
China University of Mining and Technology,
Xuzhou Jiangsu 221116, People's Republic of China
e-mail: chenhaidongcumt@hotmail.com

C. Yuan-Ping
State Key Laboratory of Coal Resources and Mine Safety,
China University of Mining and Technology,
Xuzhou Jiangsu 221116, People's Republic of China

Published online: 02 February 2013

In general, scientific issues in extraction of protective seams involve three aspects: changes in stress, damage to coal and rock, and changes in permeability. Many scholars have performed studies on these aspects using laboratory experiments. Using an X-ray CT scan, Kawakata et al. (1997) studied the process of fault formation in granite under tri-axial compression, and Zhou et al. (2008) analyzed the damage development in limestone during unloading. Bobet and Einstein (2010) and Robina et al. (1998) obtained information on the crack coalescence of plaster under uni-axial compression. The effect of stress on the permeability of coal and rock was investigated by Somerton et al. (1975), Li et al. (1997), Jasinge et al. (2011) and Wang et al. (2013). In addition, Palmer and Mansoori (1998), Shi and Durucan (2003a, b) developed models for permeability, stress and pore pressure.

According to the references, great progress has been made on extraction of protective seams from an engineering perspective, but macroscopic experiments and theoretical analysis have also been mainly emphasized. Few researches on the coupling effects among stress, damage, and permeability have been done in the laboratory. X-ray CT scanning can effectively determine internal damage development of specimens (Kawakata et al. 1997; Otani et al. 2000; Feng et al. 2004; Zhou et al. 2008), while the permeability of a specimen cannot be measured during this experiment. Therefore, based on the fact that the reduction of the three-dimensional stress on protected seams during extraction of protective seams, this paper uses X-ray CT scan experiments and permeability experiments under the same stress paths [fixed axial displacement with unloading confining pressure (FADUCP) and fixed deviatoric stress with unloading confining pressure (FDSUCP)] and the same effective confining pressure by using reconstituted coal specimens with minimal discreteness to measure damage and permeability development, respectively. Finally, damage development and its influence on the permeability of coal during unloading are analyzed by the linking of the two experimental results.

## 2 Experimental Method

### 2.1 Specimens

Due to tectonic stress, underground coal appears in a broken structure with low strength, and it is difficult to obtain a raw coal specimen. Moreover, even if a raw coal specimen can be produced, the repeatability of experiments and the ability to compare experimental results are poor (Jasinge et al. 2009, 2011; Ranjith et al. 2010). At the same time, the reconstituted coal specimens and raw coal specimens have good consistency on the deformation law (Yao and Zhou 1998; Yin et al. 2008); therefore, reconstituted coal specimens are chosen for study in this paper.

The raw materials for producing the reconstituted coal specimens consist of coking coal from the Qinan coal mine of the Huaibei coalfield in China. According to the methods of MT/T 1087-2008 (China State Administration of Work Safety 2009) and GB/T 8899-1998 (State Bureau of Quality Technology Supervision of the People's Republic of China 1998), maceral composition and proximate analysis were tested and the results are summarized in Table 1.

The production process (Peng et al. 2011) for the reconstituted coal specimens is as follows: 60–80 mesh coal particles were evenly mixed with a small amount of water and packed into abrasives to produce the reconstituted coal specimens. Next, a pressure of 100 MPa was applied for 30 min. After that, the specimens were placed in a 60 °C vacuum oven for 24 h. Finally, specimens (see Fig. 1) with an approximate height of 100 mm were obtained using a cutting machine. The physical parameters of the specimens used in the experiments are shown in Table 2.

**Table 1** Maceral composition

| Organic maceral composition | | | Inorganic maceral composition | | |
|---|---|---|---|---|---|
| Vitrinite | Inertinite | Exinite | Clay type | Sulfide | Carbonate |
| 72.94 % | 22.59 % | 0 | 4.21 % | 0.36 % | 0 |
| $R_0$ | | | 1.4243 | | |
| Proximate analysis | | | | | |
| Ash | | Volatile matter | | | Fixed carbon |
| 17.41 % | | 29.43 % | | | 51.69 % |

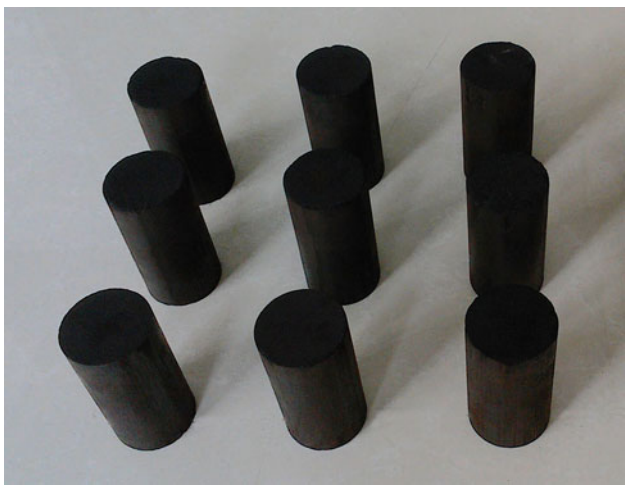

**Fig. 1** Specimens

**Table 2** Specimens physical parameters

| Specimens | Diameter (mm) | Length (mm) | Mass (g) |
|---|---|---|---|
| A | 50.9 | 100.0 | 231.16 |
| B | 50.9 | 99.4 | 236.3 |
| C | 50.7 | 100.4 | 244.89 |
| D | 50.8 | 98.5 | 237.35 |

## 2.2 Experimental Design

The experimental design used in this research is shown in Fig. 2 and described as follows. After in-site sampling and determination of basic parameters, the reconstituted coal specimens are produced. The X-ray CT scan experiments and permeability tests are performed during unloading under the same stress path and the same effective confining pressure. The CT values and CT scan images obtained from the X-ray CT scan experiments are used to analyze the damage development, and the results of the permeability tests are used to analyze the permeability variation during unloading. Because the reconstituted coal specimens with minimal discreteness are subjected to the same stress path and the same effective confining pressure, the two different experimental results can be linked to analyze the damage development and its influence on the permeability of coal during unloading.

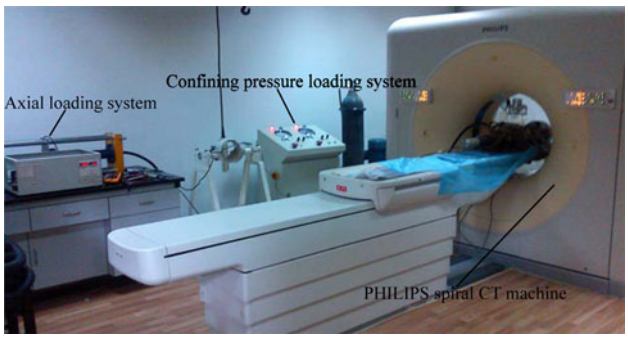


**Fig. 3** X-ray CT scan system

## 2.3 Experimental Apparatus and Experimental Procedures

### *2.3.1 X-Ray CT Scan Experiment*

Damage development in the specimens under different stress path was measured using a X-ray CT scan system (see Fig. 3) located at the Cold and Arid Regions Environmental Engineering Research Institute of the Chinese

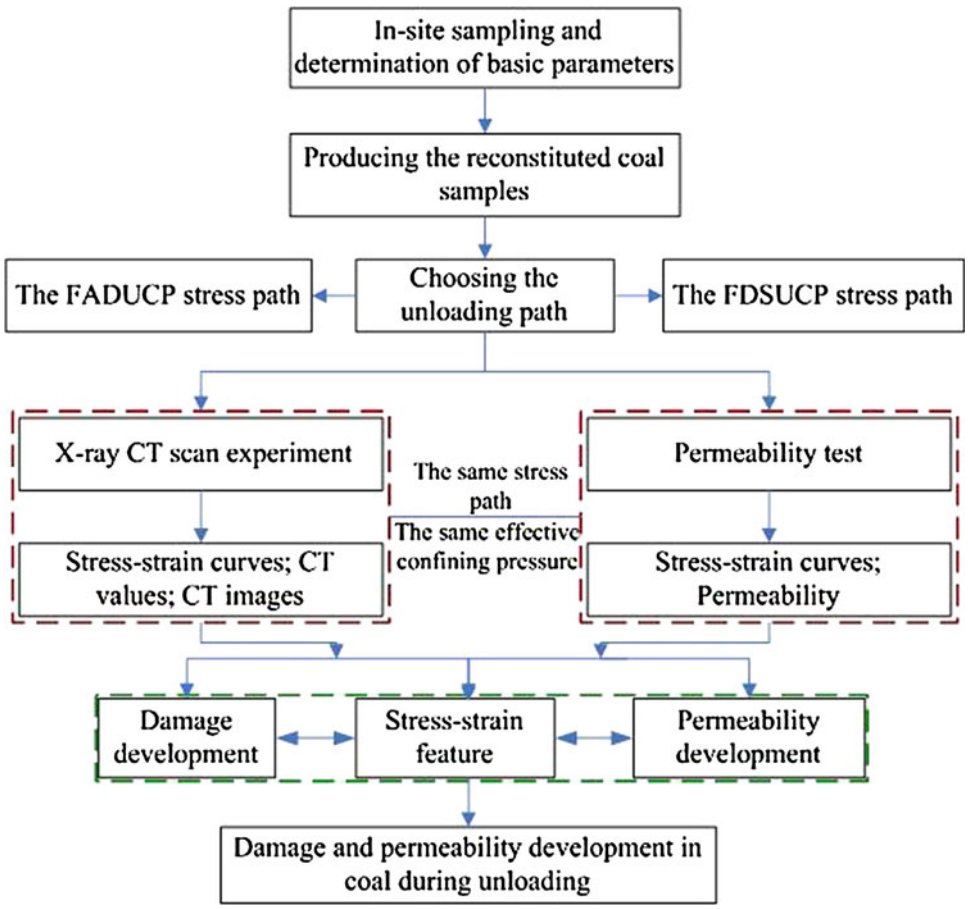


**Fig. 2** Experimental design

Academy of Sciences. This system consists of a PHILIPS spiral CT machine, a tri-axial device used to determine axial stress and axial strain, and CT image processing software. The spatial resolution of the CT machine is 0.208 × 0.208 mm, and the relative density resolution is 0.3 % Hounsfield Unit (Hu). The maximum designed axial compression and confining pressure of the tri-axial device are 200 and 20 MPa, respectively.

Specimen A and specimen B are used in the X-ray CT scan experiments under the FADUCP and FDSUCP stress paths, respectively. The experimental process uses a scan voltage of 180 mA, a scan current of 120 kV, and a scan layer thickness of 3 mm. The experimental procedure is as follows.

1. Install the specimen and conduct an X-ray CT scan at the initial stress state.
2. Gradually increase the confining pressure to 8 MPa, load the specimen to the yield point further using a 0.04 mm/min displacement loading rate, and conduct a second X-ray CT scan.
3. Conduct an X-ray CT scan on specimen A under the FADUCP stress path with an average unloading rate for the confining pressure of 0.25 MPa/min; as the confining pressure is unloaded to 6, 4.8, 3.6, 2.4, and 0.8 MPa, additional X-ray CT scans are conducted. The experiment ends when visible damage cracks can be observed from the CT images.
4. Conduct an X-ray CT scan on specimen B under the FDSUCP stress path with an average unloading rate for the confining pressure of 0.25 MPa/min; as the confining pressure is unloaded to 6, 4.8, 3.6, and 2.4 MPa, additional X-ray CT scans are conducted. The experiment ends when visible damage cracks can be observed from the CT images.

### 2.3.2 *Permeability Test*

The permeability of a specimen under different stress paths was tested using a coupling instrument to measure the stress and permeability of coal and rock (see Fig. 4). This instrument consists of a mechanical module and a fluid module. In the mechanical module, the maximum designed axial compression and confining pressure are 300 and 60 MPa, respectively. The axial deformation measurement range and radial deformation measurement range are 0–10 and 0–5 mm, respectively. In the fluid module, the range of penetration pore pressure is 0–20 MPa, and the measurement range of permeability is 0.01–100 mD.

The pressure transient method (Brace et al. 1968; Evans and Wong 1992; Wang et al. 2011) is adopted to measure

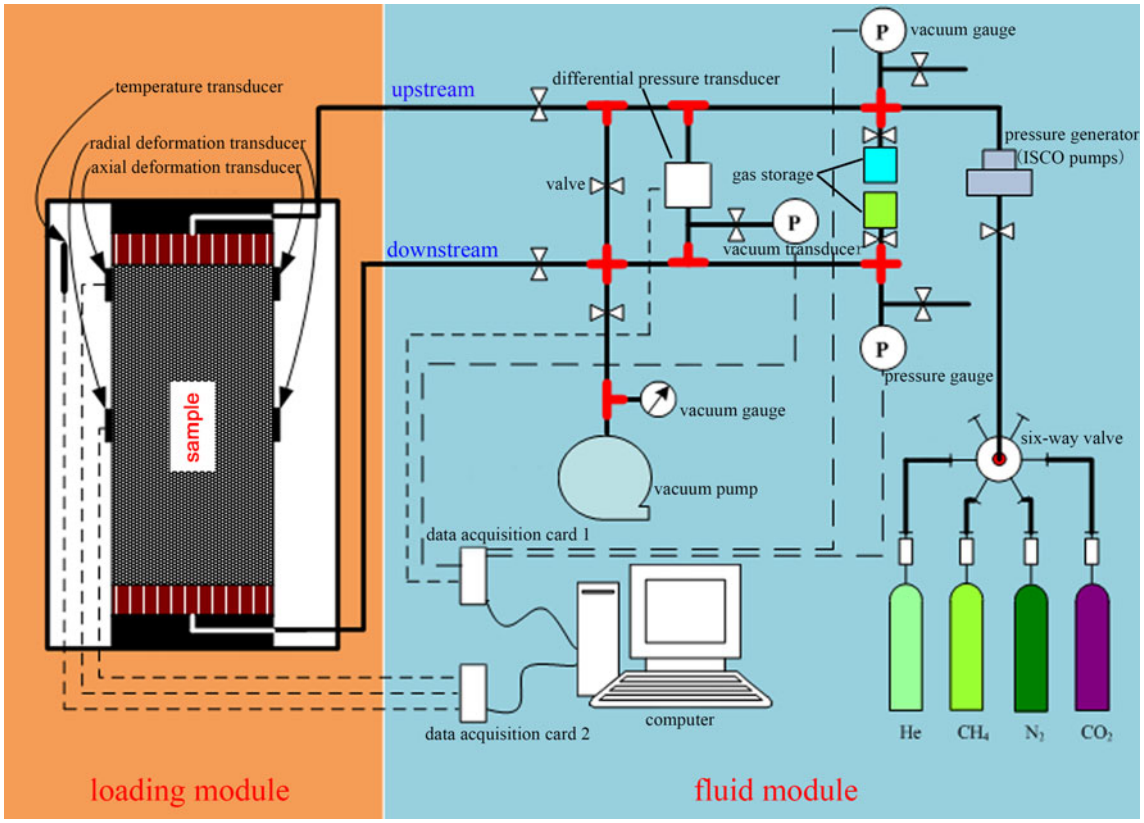


**Fig. 4** Schematic of a coupling instrument to measure the stress and permeability of coal and rock

the permeability of the specimens. The basic governing equation for the pressure pulse through a coal specimen can be written as Eqs. (1) and (2).

$$P_{\mathrm{up}}(t) - P_{\mathrm{down}}(t) = \left(P_{\mathrm{up}}(t_0) - P_{\mathrm{down}}(t_0)\right)e^{-\alpha t} \tag{1}$$

$$\alpha = (kA/\mu\beta L)\left(1/V_{\mathrm{up}} + 1/V_{\mathrm{down}}\right) \tag{2}$$

where $P_{\mathrm{up}}(t)$ and $P_{\mathrm{down}}(t)$ are the pressure of the upstream and downstream reservoirs at time $t$, respectively; $P_{\mathrm{up}}(t_0)$ and $P_{\mathrm{down}}(t_0)$ are the initial pressures of the upstream and downstream reservoirs at time $t_0$, respectively; $\alpha$ is the slope of the line when plotting the pressure decay $P_{\mathrm{up}}(t) - P_{\mathrm{down}}(t)$ on semi-log paper against time; $k$ is the permeability; $A$ and $L$ are the cross-sectional area and length of the specimen, respectively; $\mu$ and $\beta$ are the dynamic viscosity and compressibility of the gas, respectively; and $V_{\mathrm{up}}$ and $V_{\mathrm{down}}$ are the volume of the upstream reservoir and downstream reservoir, respectively.

$V_{\mathrm{up}}$ is equal to $V_{\mathrm{down}}$ in the experimental apparatus shown in Fig. 4. Thus, we obtain

$$\alpha = \frac{kA}{uL}\frac{2}{\beta V_{\mathrm{up}}} \tag{3}$$

and define

$$S_{\mathrm{up}} = \beta V_{\mathrm{up}}, \tag{4}$$

where $S_{\mathrm{up}}$, defined as the storage coefficient, indicates the change in gas volume caused by the unit gas pressure change. Thus, we obtain

$$\alpha = \frac{kA}{uL}\frac{2}{S_{\mathrm{up}}}. \tag{5}$$

Therefore, the governing equations for the experimental apparatus shown in Fig. 4 can be written as in Eqs. (1) and (5). The experimental procedure is as follows:

1. Install the specimen and gradually increase the confining pressure to 3 MPa. Apply a vacuum to the specimens for 24 h, and subsequently increase the confining pressure to 10 MPa and hold under vacuum for 6 h.
2. Set the system temperature to 40 °C and apply a gas pressure ($CH_4$; purity of 99.99 %) of 2 MPa to the specimens. Because the volume of gas in the ISCO Pump is no longer changing, we assume the adsorption equilibrium is reached.
3. Load specimen C to the yield point further using a 0.04 mm/min displacement loading velocity, and measure the permeability change during this process. Next, fixing the axial displacement and the unloading confining pressure by 0.25 MPa/min, the permeability change is measured for every 1 MPa reduction.

Load specimen D to the yield point further using a 0.04 mm/min displacement loading velocity, and measure the permeability change during this process. Next, change the control mode to load control, fixing the deviatoric stress and unloading confining pressure by 0.25 MPa/min, the permeability change is measured for every 1 MPa reduction.

## 3 Results and Analysis

### 3.1 Definition of the CT Value and Distribution of the Scanning Layers

According to Professor Hounsfield, one of the inventors of the CT machine, the CT value $H$ is defined by

$$H = 1,000 \times \frac{\mu_{\mathrm{r}}^{\mathrm{m}} - \mu_{\mathrm{w}}^{\mathrm{m}}}{\mu_{\mathrm{w}}^{\mathrm{m}}}, \tag{6}$$

where $\mu_{\mathrm{r}}^{\mathrm{m}}$ and $\mu_{\mathrm{w}}^{\mathrm{m}}$ are the mass absorption coefficients for the rock matrix material and pore water, respectively. The unit of the CT value is Hu, and 1,000 is the scaling factor for Hu. The CT values of air, water and ice are −1,000 (HU), 0 (HU), and −100 (HU), respectively. The CT value is proportional to the material density.

In this paper, the CT values were calibrated with water phantom, considering that specimens were hosted by the

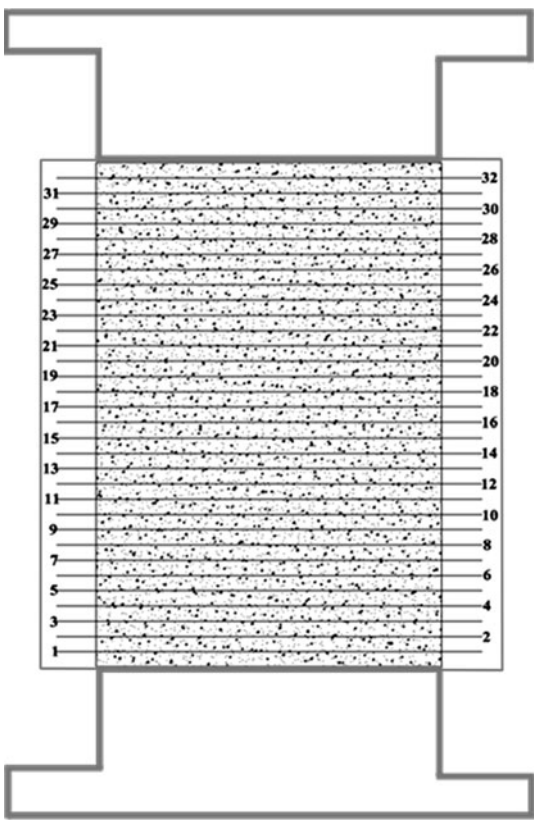


**Fig. 5** Scanning layers distribution in each scan

high-density aluminum pressure vessel during experiments and the influence of other factors, therefore, the CT values obtained from experiments did not have absolute implication. However, the CT values obtained from different stress states are relatively meaningful, and can be used to analyze the damage development of specimens. In addition, the CT images presented are related to the degree of adjusting window. Although the CT images vary with the adjusting window, the CT values do not change.

To analyze the non-uniformity of the CT value distribution in different areas in the scanning layers, this paper defines the variable Ω, which comprehensively reflects the change in the CT value and the CT variance.

$$\Omega = \frac{\mathrm{SD}}{H + 1,000} \tag{7}$$

where SD is the CT variance.

The scanning layers distribution is shown in Fig. 5, and can be divided into 32 layers.

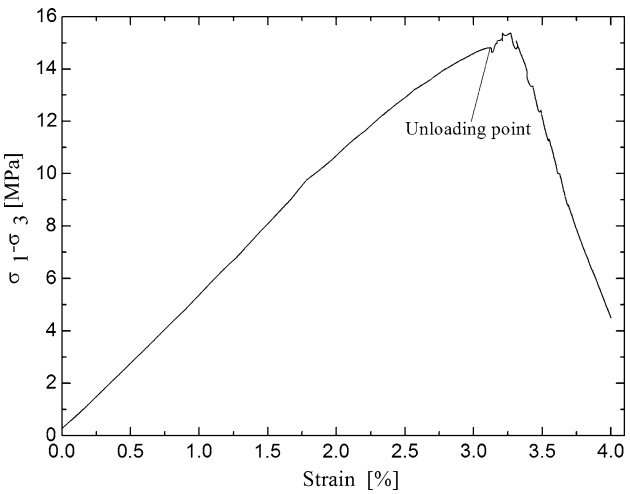


**Fig. 6** Relation between stress and strain under the FADUCP stress path

## 3.2 Fixing Axial Displacement with Unloading Confining Pressure

### *3.2.1 Analysis of Damage Development During Unloading*

The stress–strain curves under the FADUCP stress path are shown in Fig. 6. At the unloading point, the deviatoric stress and strain are 14.65 MPa and 3.13 %, respectively. As the confining pressure is unloaded from 8 to 6 MPa at a fast rate, the deviatoric stress increases slightly. The peak of the deviatoric stress occurs at 15.37 MPa with a strain of 3.21 %. Subsequently, the deviatoric stress begins to decrease during unloading of the confining pressure, and at the same time, the axial strain also increases slightly.

Table 3 and Fig. 7 show the changes in the CT values and CT images obtained under the FADUCP stress path. There are many scanning layers in each scan, and the 8th, 16th, and 25th layers are typical representatives to be analyzed here. Seen from Table 3, the change in CT values is small as the confining pressure changed from 8 to 6 MPa, which implies that damage to the specimen during this process is not extensive. Therefore, for brevity, Fig. 7 shows only the CT images for confining pressures from 4.8 to 0.8 MPa. The damage evolution process is as follows.

1. Initial scanning (1st scan) is carried out before loading. The difference in the initial damages determines that of the CT value of each scanning layer.
2. When the confining pressure reaches 8 MPa and the deviatoric stress reaches 14.65 MPa (2nd scan), compared with the initial scanning, the CT value of the 8th scanning layer increases by 54.8, the 16th increases by 52.4 and the 25th increases by 53.9, which means the specimen is consolidated.
3. When the confining pressure is 6 MPa and the deviatoric stress reaches 15.37 MPa (3rd scan), compared with the 2nd scan, the CT values of the 8th, 16th, and 25th scanning layers are reduced by 1.7, 1.5, and 2.6, respectively, which means that damage to the specimen is occurred.

**Table 3** The variation of CT values during FADUCP

| Scan no. | Confining pressure (MPa) | $\sigma_1 - \sigma_3$ (MPa) | 8th scanning layer | | 16th scanning layer | | 25th scanning layer | |
|---|---|---|---|---|---|---|---|---|
| | | | *H* | SD | *H* | SD | *H* | SD |
| 1 | 0.0 | 0.0 | 224.3 | 27.4 | 198.0 | 25.5 | 172.7 | 24.6 |
| 2 | 8.0 | 14.65 | 279.1 | 58.4 | 250.4 | 73.7 | 226.6 | 89.3 |
| 3 | 6.0 | 15.37 | 277.4 | 26.3 | 248.9 | 21.7 | 224 | 20.6 |
| 4 | 4.8 | 14.89 | 272.5 | 88.7 | 242.9 | 101.4 | 218.5 | 103.5 |
| 5 | 3.6 | 13.25 | 269.4 | 27 | 236 | 21.2 | 213.6 | 20 |
| 6 | 2.4 | 11.33 | 266.5 | 27.4 | 223.2 | 22.4 | 199 | 21.3 |
| 7 | 0.8 | 4.79 | 251.7 | 28.8 | 199.2 | 30.4 | 176.1 | 33.3 |

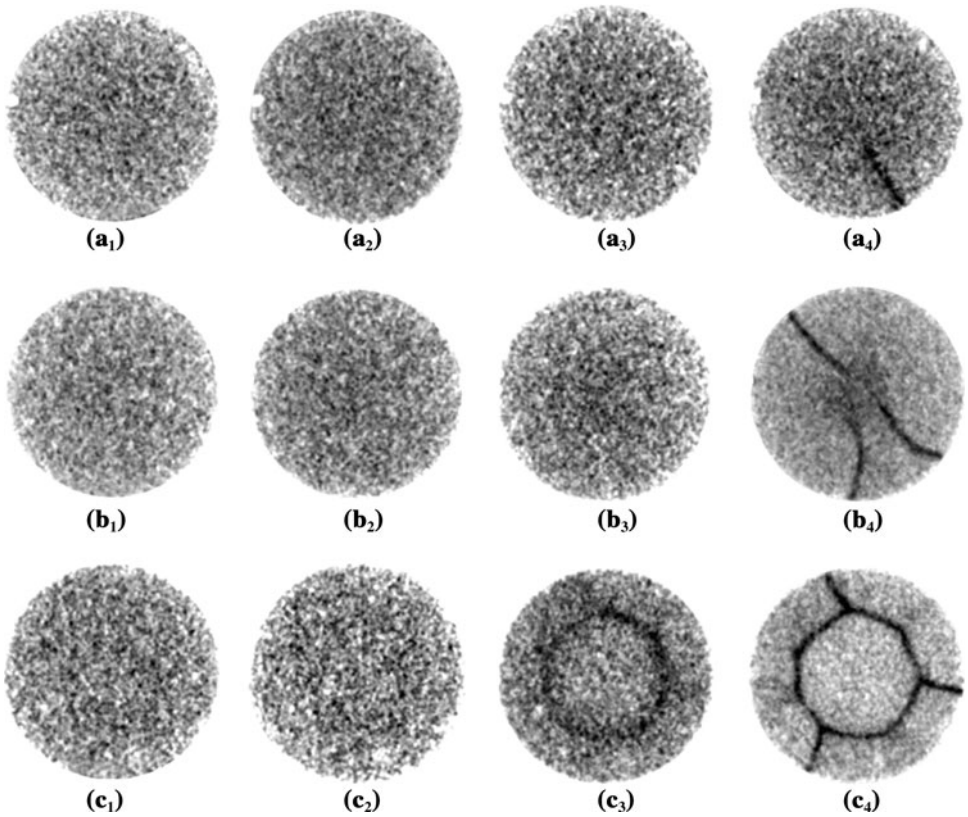


**Fig. 7** Variation of CT images in the different stress states. $\mathbf{a_1}$–$\mathbf{a_4}$, $\mathbf{b_1}$–$\mathbf{b_4}$, $\mathbf{c_1}$–$\mathbf{c_4}$ are the CT images of the 8th, 16th and 25th scanning layers with the confining pressure being 4.8, 3.6, 2.4, 0.8 MPa, respectively

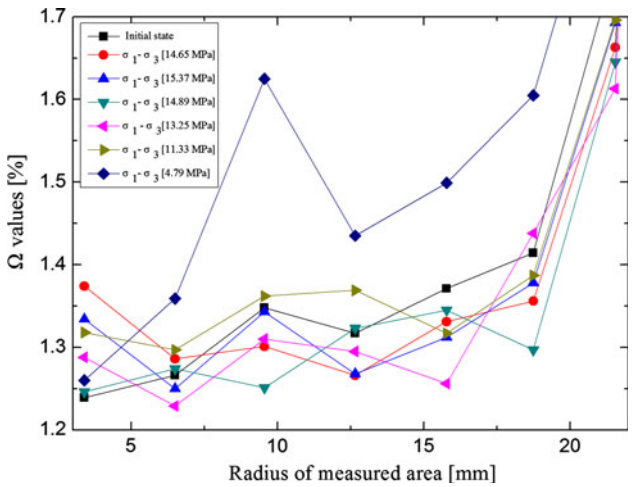


**Fig. 8** Ω values of the 8th scanning layer in different measured area. The radius of measured area is the distance from the edge to the center

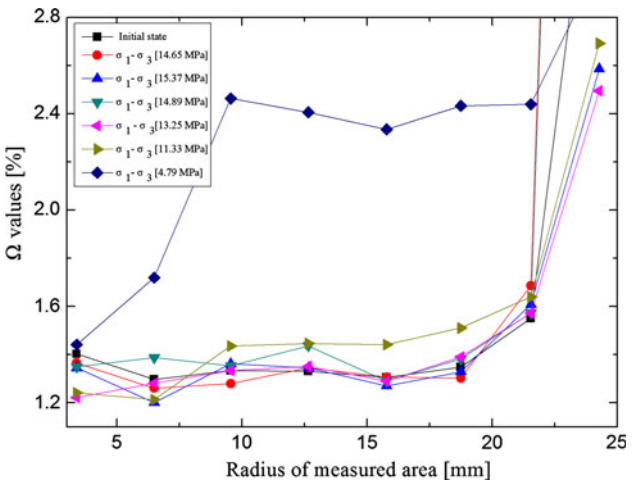


**Fig. 9** Ω values of the 16th scanning layer in different measured area. The radius of measured area is the distance from the edge to the center

4. When the confining pressure is 4.8 MPa and the deviatoric stress reaches 14.89 MPa (4th scan; Fig. 7 $a_1$, $b_1$, $c_1$), compared with the 3rd scan, the CT values of the 8th, 16th, and 25th scanning layers are reduced by 4.9, 6.0, and 5.5, respectively, which means that the damage to the specimen continues to develop.

5. When the confining pressure is 3.6 MPa and the deviatoric stress reaches 13.25 MPa (5th scan; Fig. 7$a_2$, $b_2$, $c_2$), compared with the 4th scan, the CT values of the 8th, 16th, and 25th scanning layers is reduced by 3.1, 6.9, and 4.4, respectively, which means that the damage to the specimen accumulates gradually.

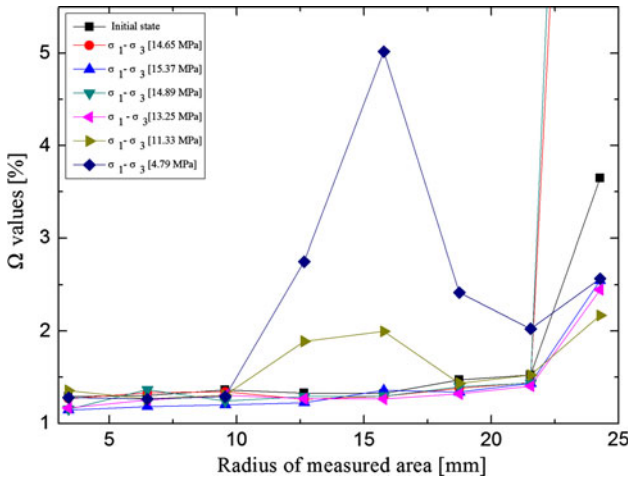


**Fig. 10** Ω values of the 25th scanning layer in different measured area. The radius of measured area is the distance from the edge to the center

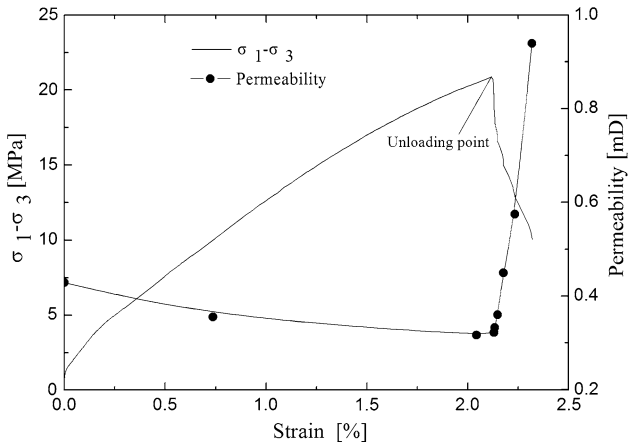


**Fig. 11** Relationship among the deviatoric stress, permeability and strain under the FADUCP stress path

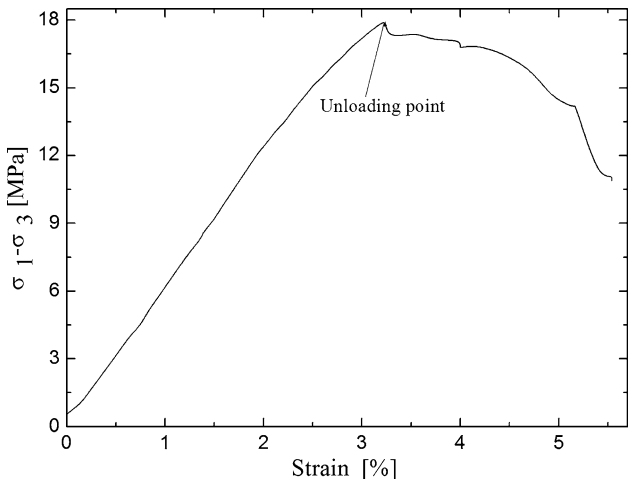


**Fig. 12** Relation between stress and strain under the FDSUCP stress path

6. When the confining pressure is 2.4 MPa and the deviatoric stress reaches 11.33 MPa (6th scan; Fig. 7$a_3$, $b_3$, $c_3$), compared with the 5th scan, the CT values of the 16th and 25th scanning layers are reduced by 12.8 and 32.6, respectively, and the CT value of the 8th scanning layer is reduced by 4.4. It can be observed from the CT images that obvious damage areas appear in the 16th and 25th scanning layers, particularly the ring-shaped damage cracks in the 25th scanning layer.
7. When the confining pressure is 0.8 MPa and the deviatoric stress reaches 4.79 MPa (7th scan; Fig. 7$a_4$, $b_4$, $c_4$), compared with the 6th scan, the CT values of the 8th, 16th, and 25th scanning layers are reduced by 14.8, 24.0, and 22.9, respectively. It can be observed from the CT images that damage cracks also appear in the 8th and 16th scanning layers at the same time that the ring-shaped damage cracks of the 25th scanning layer develop outward.

To further analyze the damage development of the different regions in each scanning layer during unloading, the Ω values reflecting the non-uniformity of the distribution of the CT values are calculated using Eq. (7). Figures 8, 9 and 10 show that, in the process of unloading, the Ω values change in the local areas and increase suddenly for the stress state that results when the confining pressure is unloaded to 0.8 MPa and the deviatoric stress reaches 4.79 MPa. According to the CT images, the damage cracks appear in those local areas. However, due to the influence of convolution artifacts during CT imaging, the Ω values at the edge of specimen, which are also large, cannot be used for analysis.

### *3.2.2 Permeability Changes During Unloading*

The results of the permeability tests are shown in Fig. 11. When the specimen is in the stress state of hydrostatic pressure, at the same time, the effective confining pressure is 8 MPa, the initial permeability is 0.429 mD. Maintaining the effective confining pressure at 8 MPa, as the specimen is loaded to the unloading point, the permeability is gradually reduced. Under the FADUCP stress path, the permeability of the unloading point is not measured, and the permeability in the vicinity is 0.316 mD. During the initial period of unloading, the permeability increases slowly. When the effective confining pressure is unloaded with the deviatoric stress reduced to 7 and 6 MPa, the permeability increases to only 0.322 and 0.332 mD, respectively. After the effective confining pressure reaches 5 MPa, the growth rate of the permeability begins to increase. When the effective confining pressure is unloaded to 5, 4, 3 and 2 MPa, the permeability increases to 0.360, 0.450, 0.574 and 0.939 mD, respectively.

**Table 4** Variation of CT values during FDSUCP

| Scan no. | Confining pressure (MPa) | $\sigma_1 - \sigma_3$ (MPa) | 6th scanning layer | | 15th scanning layer | | 23rd scanning layer | |
|---|---|---|---|---|---|---|---|---|
| | | | *H* | SD | *H* | SD | *H* | SD |
| 1 | 0 | 0 | 184.0 | 21.6 | 208.6 | 22.3 | 234.3 | 22.1 |
| 2 | 8 | 17.84 | 237.3 | 20.1 | 257.8 | 21.8 | 281.4 | 21.3 |
| 3 | 6 | 17.73 | 233.1 | 19.8 | 252.3 | 21.5 | 277 | 21.4 |
| 4 | 4.8 | 17.13 | 224.3 | 19.2 | 244.2 | 21.4 | 274.4 | 21 |
| 5 | 3.6 | 14.29 | 206.7 | 21.9 | 226.3 | 21 | 270.8 | 22 |
| 6 | 2.4 | 10.89 | 195.6 | 27.5 | 207.3 | 23.8 | 259.9 | 22.4 |

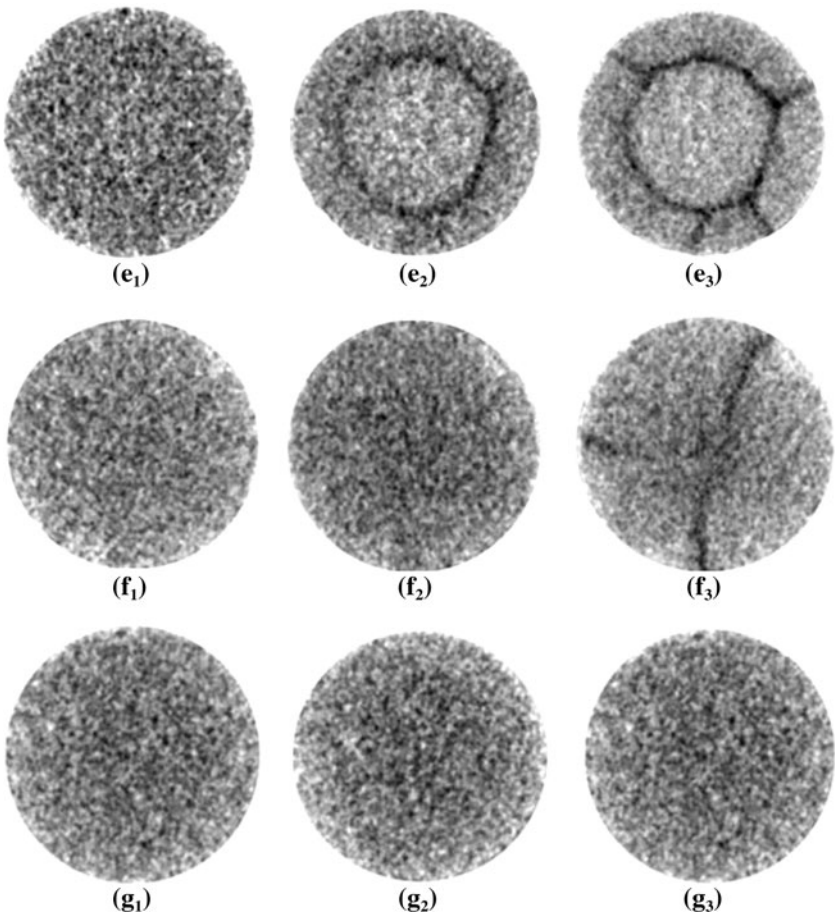


**Fig. 13** Variation of CT images in the different stress states. **e1–e3**, **f1–f3**, **g1–g3** are the CT images of the 6th, 15th and 23rd scanning layers with the confining pressure being 4.8, 3.6, 2.4 MPa, respectively

## 3.3 Fixing Deviatoric Stress with Unloading Confining Pressure

### *3.3.1 Analysis of Damage Development During Unloading*

The stress–strain curves under the FDSUCP stress path is shown in Fig. 12. Due to specimen error, the stress states of the yield point show small differences with that shown in Fig. 6. At the unloading point, the deviatoric stress and strain are 17.84 MPa and 3.19 %, respectively. Before the confining pressure is unloaded to 6 MPa, the deviatoric stress can be maintained as approximately constant. After that, the deviatoric stress begins to decrease while the axial strain grows rapidly.

Table 4 and Fig. 13 show the changes in the CT values and the CT images obtained, respectively, under the FDSUCP stress path. This paper selects the 6th layer, 15th layer and 23rd layer as representative for analysis. Additionally, for brevity, Fig. 13 shows only the CT images for the confining pressure unloaded from 4.8 to 2.4 MPa. The damage evolution process is as follows.

1. Initial scanning (first scan) is carried out before loading; the difference in the initial damages determines that of the CT value of each scanning layer.
2. When the confining pressure is 8 MPa and the deviatoric stress reaches 17.84 MPa (second scan), compared with the initial scan, the CT value of the 6th scanning layer increases by 53.3, the CT value of the 15th scanning layer increases by 49.2, and the CT value of the 23rd scanning layer increases by 47.1, which means that the specimen is consolidated.
3. When the confining pressure is 6 MPa and the deviatoric stress reaches 17.73 MPa (third scan); compared with the second scanning, the CT values of the 6th, 15th, and 23rd scanning layers are reduced by 4.2, 5.5, and 4.4, respectively, which means that damage to the specimen begins to appear.
4. When the confining pressure is 4.8 MPa and the deviatoric stress reaches 17.13 MPa (fourth scan; Fig. 13$e_1$, $f_1$, $g_1$), compared with the third scan, the CT values of the 6th, 15th, and 23rd scanning layers are by reduced 8.8, 8.1, and 2.6, respectively, which means that damage to the specimen continues to develop.
5. When the confining pressure is 3.6 MPa and the deviatoric stress reaches 14.29 MPa (fifth scan; Fig. 13$e_2$, $f_2$, $g_2$), compared with the 4th scan, the CT value of the 6th and 15th scanning layers is reduced by 17.6 and 17.9, respectively, and the CT value of the 23rd scanning layer is reduced by 3.6. It can be observed from the CT images that obvious damage areas appear in the 6th and 15th scanning layers, particularly the ring-shape damage cracks identical to Fig. 7$c_3$ in the 6th scanning layer.
6. When the confining pressure is 2.4 MPa and the deviatoric stress reaches 10.89 MPa (6th scan; Fig. 13$e_3$, $f_3$, $g_3$), compared with the fifth scan, the CT values of the 6th, 15th, and 23rd scanning layers are reduced by 11.1, 19.0, and 10.9, respectively. It can be observed from the CT images that damage cracks also appear in the 15th scanning layer at the same time that ring-shaped damage cracks develop outward in the sixth scanning layer.

According to the CT values and the CT variances of different areas measured in each scan, the Ω values reflecting the non-uniformity of the distribution of CT values are calculated using Eq. (7). As shown in Figs. 14, 15 and 16, in contrast with the CT images, similar to the results of the FADUCP stress path, the Ω values of the local area obviously increase when damage cracks emerge in the local areas. Additionally, due to the influence of convolution artifacts during the CT imaging, the Ω values at the edge of specimen are large and cannot be used for analytical purposes.

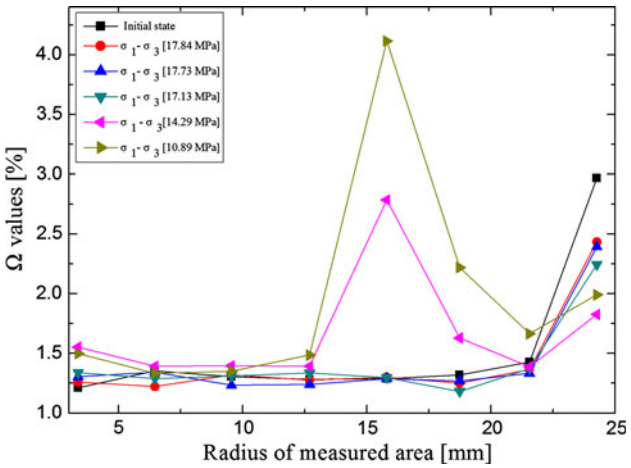


**Fig. 14** Ω values of the 6th scanning layer in different measured area. The radius of measured area is the distance from the edge to the center

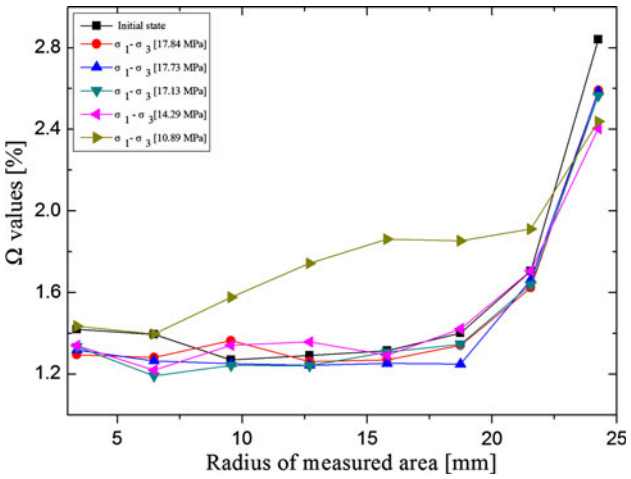


**Fig. 15** Ω values of the 15th scanning layer in different measured area. The radius of measured area is the distance from the edge to the center

### *3.3.2 Permeability Changes During Unloading*

The results of the permeability test are shown in Fig. 17. When the specimen is in the stress state of hydrostatic pressure, at the same time, the effective confining pressure is 8 MPa, the initial permeability of the specimen is 0.31 mD. Maintaining the effective confining pressure at 8 MPa, as the specimen is loaded to the unloading point, the permeability is gradually reduced. The permeability at the unloading point is 0.163 mD, when the effective confining pressure is unloaded to 7 and 6 MPa, together with the decrease in the deviatoric stress, the permeability increases to 0.190 and 0.199 mD, respectively. As the unloading continues, after the stress state that results when the effective confining pressure reaches 5 MPa, the growth

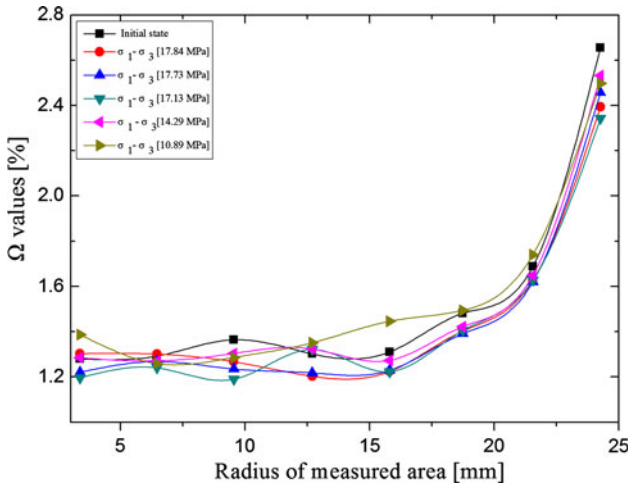


**Fig. 16** Ω values of the 23rd scanning layer in different measured area. The radius of measured area is the distance from the edge to the center

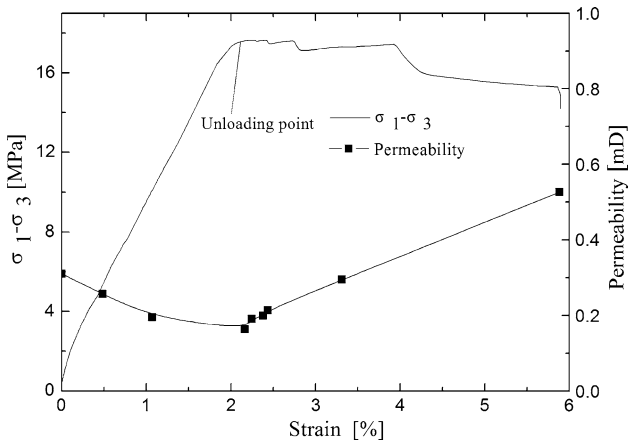


**Fig. 17** Relationship among deviatoric stress, permeability and strain under the FDSUCP stress path

rate of the permeability begins to increase. When the effective confining pressure is unloaded to 5, 4 and 3 MPa, the permeability increases to 0.213, 0.295 and 0.526 mD, respectively.

## 4 Discussion

### 4.1 Analysis of the Damage Difference

The CT values of the 8th, 16th, and 25th scanning layers in the initial scanning under the FADUCP stress path are 224.3, 198.0, and 172.7, respectively, and that of the CT values of the 6th, 15th, and 23rd scanning layers in the initial scan under the FDSUCP stress path are 184.0, 208.6, and 234.3, respectively. Since the CT value is a reflection of the density, it can be inferred that the 8th scanning layer has the largest initial density, the 16th the second and the 25th the smallest for the specimen under the FADUCP stress path. Similarly, the 23rd, the largest, followed by the 15th, and the 6th, the smallest for the specimen under the FDSUCP stress path.

It can be observed from the CT values and CT images that the damage to the 25th scanning layer is maximal and to the 8th is minimal under the FADUCP stress path. Similarly, the damage to the 6th is maximal and to the 23rd is minimal under the FDSUCP stress path.

Therefore, the correspondence between the CT values, the CT images and the damage development in the different scanning layers indicates that the differences in density cause the differences in damage among the scanning layers. Additionally, the smaller the CT values of the scanning layer, the more severe the damage develops.

### 4.2 Effect of the Stress Path on the Damage and Permeability

Damage and permeability are sensitive to stress, and the inconsistency of the stress path leads to differences in damage and permeability development.

When the damage cracks appear (Figs. 7$c_3$, 13$e_2$), compared with the unloading point, the deviatoric stress under the FADUCP stress path decreases by 23.1 % while the deviatoric stress under the FDSUCP stress path decreases by 19.9 %. However, when the effective confining pressures are all unloaded from 8 to 3 MPa, compared with the unloading point, the deviatoric stress under the FADUCP and FDSUCP stress paths decrease separately by 36.6 and 14.2 %, respectively; however, the permeability under the FDSUCP stress path increases by 222.5 %, and the permeability under the FADUCP stress path increases by 81.5 % compared with the permeability at the vicinity of the unloading point. Therefore, we can conclude that the FDSUCP stress path causes greater damage to the specimen than that of the FADUCP.

### 4.3 Effect of Damage Development on Permeability

Due to instrument error, specimen error, adsorption of gas in coal etc., the stress–strain curves obtained from the X-ray CT scan experiment and permeability experiment under the same stress path are different. However, the shapes appear to be quite similar. This similarity verifies the feasibility of the experiment design. The results obtained separately from the X-ray CT scan experiment and the permeability experiments are linked together to analyze the damage development and its effect on the permeability of the reconstituted coal specimens.

To directly study the effect of damage to the coal body on permeability, it is necessary to calculate the damage variable.

The CT values reflect the density of the material; and also, as shown in Eq. (8) (Yang et al. 1998), the damage variable can be expressed by the change in the material density; therefore, we can attempt to build a relationship between the CT value and the damage variable.

$$D = \frac{1}{m_0^2}\frac{\Delta\rho}{\rho_{\text{initial}}}, \tag{8}$$

where $D$ is the specimen damage variable; $m_0$ is the space resolution of the CT machine, and $\rho_{\text{initial}}$ is the initial density, and $\Delta\rho$ is the change in density.

The CT value is proportional to the mass-absorption coefficient, hence

$$H = \lambda\mu, \tag{9}$$

where $H$ and $\mu$ are the CT value and mass absorption coefficient, respectively, and $\lambda$ is the proportion coefficient.

Because only air exists in the specimen, $\mu$ can be expressed as (Feng et al. 2004; Zhou et al. 2008).

$$\mu = \mu_{\text{m}}\rho = (1-\phi)\rho_{\text{r}}\mu_{\text{r}}^{\text{m}} + \phi\rho_{\text{a}}\mu_{\text{a}}^{\text{m}}, \tag{10}$$

where $\rho_{\text{r}}$ and $\rho_{\text{a}}$ are the density of the coal matrix and air, respectively, $\mu_{\text{r}}^{\text{m}}$ and $\mu_{\text{a}}^{\text{m}}$ are the mass absorption coefficient of the coal matrix and air to the X-ray, respectively, and $\phi$ is the porosity.

According to Eq. (10)

$$\phi = \frac{\mu - \rho_{\text{r}}\mu_{\text{r}}^{\text{m}}}{\rho_{\text{a}}\mu_{\text{a}}^{\text{m}} - \rho_{\text{r}}\mu_{\text{r}}^{\text{m}}}. \tag{11}$$

From Eqs. (9), (10) and (11), we obtain

$$\phi = \frac{H_{\text{r}} - H}{H_{\text{r}} - H_{\text{a}}}, \tag{12}$$

where $H_{\text{r}}$ and $H_{\text{a}}$ are the CT values of rock matrix material and air, respectively, and $\rho$ can be expressed as

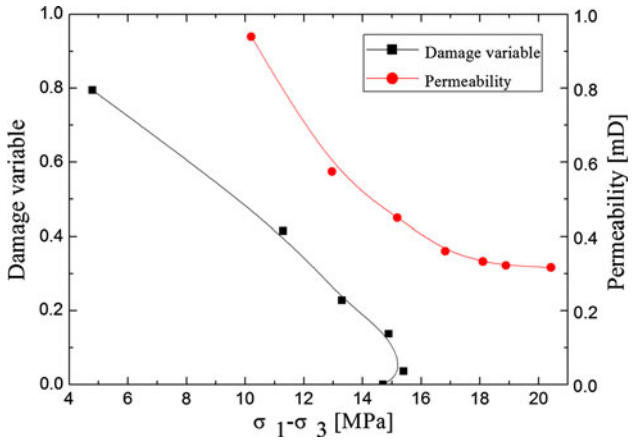


**Fig. 18** Relationship among damage variable, permeability and deviatoric stress under the FADUCP stress path

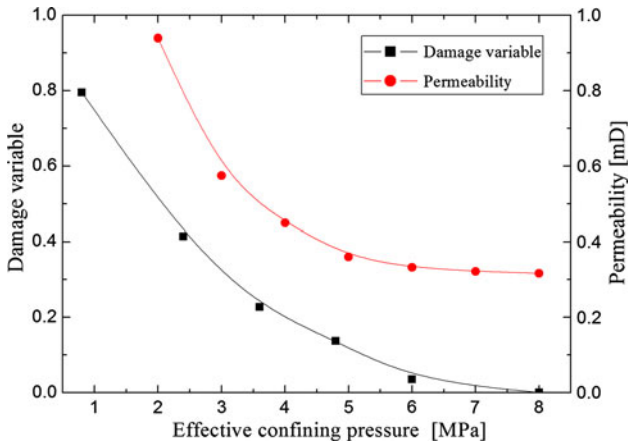


**Fig. 19** Relationship among damage variable, permeability and effective confining pressure under the FADUCP stress path

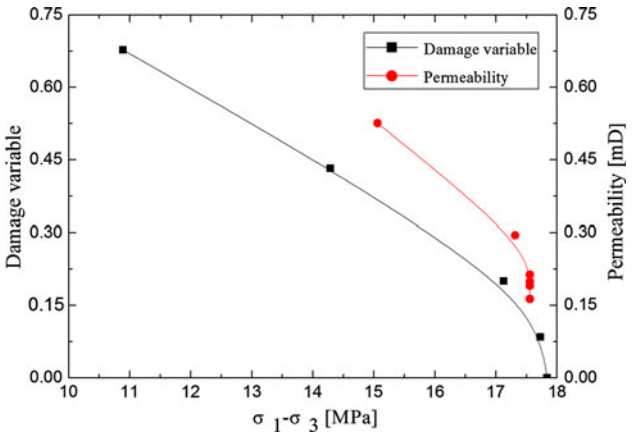


**Fig. 20** Relationship among damage variable, permeability and deviatoric stress under the FDSUCP stress path

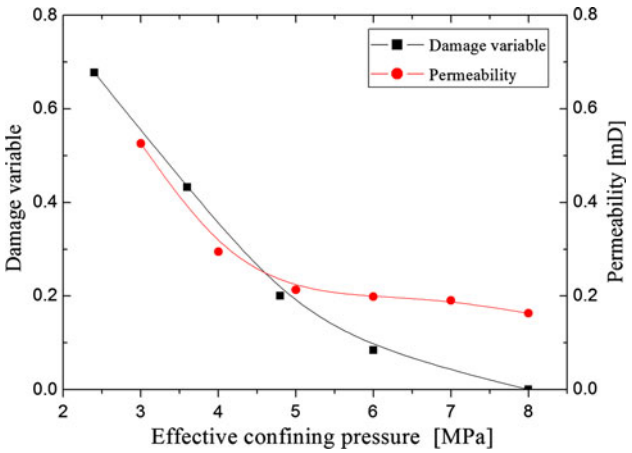


**Fig. 21** Relationship among damage variable, permeability and effective confining pressure under the FDSUCP stress path

$$\rho = (1 - \phi)\rho_r + \phi\rho_a. \quad (13)$$

If the small amount of air within the specimen is ignored, $\rho$ can be simplified as

$$\rho = (1 - \phi)\rho_r \quad (14)$$

According to Eqs. (12) and (14), the following expression can be obtained as

$$\rho = \frac{H - H_a}{H_r - H_a}\rho_r. \quad (15)$$

Because $H_a = -1,000$, hence

$$\rho = \frac{H + 1,000}{H_r + 1,000}\rho_r \quad (16)$$

Substituting Eq. (16) into Eq. (8), we obtain

$$D = \frac{1}{m_0^2}\left(\left(\frac{H + 1000}{H_r + 1000}\rho_r\right) - \rho_{initial}\right). \quad (17)$$

When the small amount of air within the specimen is ignored, the matrix densities of specimen A and specimen B are approximately 1.136 and 1.1683 g/cm$^3$, respectively. Therefore, according to the mean CT values at the unloading point, we can obtain the mean matrix density of specimens at this stress state by Eq. (16). This paper primarily studies the damage and permeability development during unloading, and therefore the damage variable of the unloading point is viewed as 0. $m_0$ is 0.028. Finally, based on the mean CT values, damage variable during unloading can be calculated by Eqs. (16) and (17).

The damage variable and permeability are obtained separately from the X-ray CT scan experiments and permeability tests. It can be seen in Figs. 18, 19, 20 and 21 that the trends in the changes are approximately consistent under the same stress path during unloading. When the effective confining pressure is unloaded from 8 to 6 MPa, the damage variable under the FADUCP and FDSUCP stress paths increases, respectively to 0.0351 and 0.084, while the permeability (compared with the unloading point) increases by 1.7 and 16.7 %, respectively. In addition, this results shows that the damage variable and permeability increases are rather small. After the effective confining pressure is unloaded together with the decrease in the deviatoric stress, the increases in the damage variable and permeability begin to accelerate. This observation provides a guideline for the development of CBM resources in coal seam groups with low permeability.

## 5 Conclusions

This paper studies the damage and permeability development in reconstituted coal specimens with an initial effective confining pressure of 8 MPa during unloading under the FADUCP and FDSUCP stress paths. When the effective confining pressure is unloaded from 8 to 6 MPa, compared with the unloading point under the FADUCP and FDSUCP stress paths, the damage variable and permeability increase by 0.0351 and 0.084, respectively; at the same time, the permeability increases by 1.7 and 16.7 %, respectively; these results indicate that the damage variable and permeability increased notably little in this process. As the effective confining pressure is unloaded to approximately 5 MPa, together with the decrease in the deviatoric stress, the growth of the damage variable and permeability begin to accelerate. The damage in specimens under the FDSUCP stress path is even larger than that from the FADUCP stress path. When the damage cracks appear in the specimens, compared with the unloading point, the decrease in the deviatoric stress under the FDSUCP stress path is 19.9 % and the decrease of the deviatoric stress under the FADUCP stress path is 23.1 %. Additionally, when the effective confining pressure is unloaded from 8 to 3 MPa, and the deviatoric stress under the FADUCP and FDSUCP stress paths decrease separately by 36.6 and 14.2 %, respectively; however, the permeability under the FADUCP stress path increases by approximately 81.5 % and the permeability under the FDSUCP stress path increases by 222.5 %.

**Acknowledgments** This research was supported by the Natural Science Foundation for the Youth of China (No. 51204173), the National Basic Research Program of China (973 Program, No. 2011CB201204) and the Natural Science Foundation for the Youth of China (No. 41202118).

## References

Bobet A, Einstein HH (2010) Fracture coalescence in rock-type materials under uniaxial and biaxial compression. Int J Rock Mech Min Sci 35:863–888

Brace WF, Walsh JB, Frangos WT (1968) Permeability of granite under high pressure. J Geophys Res 73:2225–2236

China State Administration of Work Safety (2009) MT/T 1087-2008 test methods for proximate analysis of coal by instruments. Beijing (in Chinese)

Evans B, Wong TF (1992) Fault mechanics and transport properties of rocks. Academic Press, New York

Feng XT, Chen SL, Zhou H (2004) Real-time computerized tomography (CT) experiments on sandstone damage evolution during triaxial compression with chemical corrosion. Int J Rock Mech Min Sci 41:181–192

Guo H, Yuan L, Shen BT, Qu DD, Xue JH (2012) Mining-induced strata stress changes, fractures and gas flow dynamics in multi-seam longwall mining. Int J Rock Mech Min Sci 54:129–139

Jasinge D, Ranjith PG, Choi SK, Kodikara J, Arthur M, Li H (2009) Mechanical properties of reconstituted Australian black coal. J Geotech Geoenviron Eng 135:980–985

Jasinge D, Ranjith PG, Choi SK (2011) Effects of effective stress changes on permeability of Latrobe valley brown coal. Fuel 90:1292–1300

Karacan CÖ, Esterhuizen GS, Schatzel S, Diamond WP (2007) Reservoir simulation based modeling for characterizing longwall

methane emissions and gob gas venthole production. Int J Coal Geol 71:225–245

Kawakata H, Cho A, Yanagidani T, Shimada M (1997) The observations of faulting in westerly granite under triaxial compression by X-ray CT scan. Int J Rock Mech Min Sci 34: 151.e1–151.e12

Lama RD, Bodziony J (1998) Management of outburst in underground coal mines. Int J Coal Geol 35:83–115

Li SP, Wu DX, Xie WD, Li YS, Wu ZY, Zhou G, Zhao HY (1997) Effect of confining pressure, pore pressure and specimen dimension on permeability of Yinzhuang sandstone. Int J Rock Mech Min Sci 34:175

Liu YK, Zhou FB, Liu L, Liu C, Hu SY (2011) An experimental and numerical investigation on the deformation of overlying coal seams above double-seam extraction for controlling coal mine methane emissions. Int J Coal Geol 87:139–149

Majdi A, Hassani FP, Nasiri MY (2012) Prediction of the height of destressed zone above the mined panel roof in longwall coal mining. Int J Coal Geol 98:62–72

Otani J, Mukunoki T, Obara Y (2000) Application of X-ray CT method for characterization of failure in soils. Soils Found 40:113–120

Palchik V (1989) Analytical and empirical prognosis of rock foliation in rock masses. J Coal Ukraine 7:45–46

Palchik V (2003) Formation of fractured zones in overburden due to longwall mining. Environ Geol 44:28–38

Palchik V (2005) Localization of mining-induced horizontal fractures along rock layer interfaces in overburden: field measurements and prediction. Environ Geol 48:68–80

Palmer I, Mansoori J (1998) How permeability depends on stress and pore pressure in coalbeds: a new model. SPE Reserv Eval Eng 1:539–544

Peng SJ, Xu J, Yang HW, Liu D (2011) Experimental study on the influence mechanism of gas seepage on coal and gas outburst disaster. Saf Sci 50:816–821

Ranjith PG, Jasinge D, Choi SK, Mehic M, Shannon B (2010) The effect of $CO_2$ saturation on mechanical properties of Australian black coal using acoustic emission. Fuel 89:2110–2117

Shi JQ, Durucan S (2003) Changes in permeability of coalbeds during primary recovery—part 1: model formulation and analysis. Proceedings of the 2003 International Coalbed Methane Symposium. University of Alabama, Tuscaloosa, Paper 0341

Shi JQ, Durucan S (2003) Changes in permeability of coalbeds during primary recovery—part 2: model formulation and analysis. Proceedings of the 2003 International Coalbed Methane Symposium. University of Alabama, Tuscaloosa, Paper 0342

Somerton WH, Soylemezocjlu IM, Dudley RC (1975) Effect of stress on permeability of coal. Int J Rock Mech Min Sci Geomech Abstr 12:129–145

State Bureau of Quality Technology Supervision of the People's Republic of China (1998) Determination of maceral group composition and minerals in coal, China. Standard Press, Beijing (in Chinese)

Wang L, Cheng YP (2012) Drainage and utilization of Chinese coal mine methane with a coal-methane co-exploitation model: analysis and projections. Resour Policy 37:315–321

Wang SG, Elsworth D, Liu JS (2011) Permeability evolution in fractured coal: the roles of fracture geometry and water-content. Int J Coal Geol 87:13–25

Wang SG, Elsworth D, Liu JS (2013) Permeability evolution during progressive deformation of intact coal and implications for instability in underground coal seams. Int J Rock Mech Min Sci 58:34–45

Wong RHC, Chau KT (1998) Crack coalescence in a rock-like material containing two cracks. Int J Rock Mech Min Sci 35: 147–164

Yang GS, Xie DY, Zhang CQ (1998) Quantitative analysis of CT distribution law of rock damage. Chin J Rock Mech Eng 17:279–285 (in Chinese)

Yang TH, Xu T, Tang CA, Shi BM, Yu QX (2011) Stress-damage-flow coupling model and its application to pressure relief coal bed methane in deep coal seam. Int J Coal Geol 86:357–366

Yang W, Lin BQ, Qu YA, Zhao S, Zhao C, Jia LL, Zhao WQ (2011a) Mechanism of strata deformation under protective seam and its application for relieved methane control. Int J Coal Geol 85:300–306

Yang W, Lin BQ, Qu YA, Li ZW, Zhai C, Jia LL, Zhao WQ (2011b) Stress evolution with time and space during mining of a coal seam. Int J Rock Mech Min Sci 48:1145–1152

Yao YP, Zhou SN (1998) The mechanical property of coal containing gas. J China Univ Min Technol 1:1–7

Yin GZ, Wang DK, Zhang DM, Wang WZ (2008) Test analysis of deformation characteristics and compressive strengths of two types of coal specimens containing gas. Chin J Rock Mech Eng 28:410–417 (in Chinese)

Zhou XP, Zhang YX, Ha QL (2008) Real-time computerized tomography (CT) experiments on limestone damage evolution during unloading. Theor Appl Fract Mech 50:49–56